Scaling laws of nanoporous metals under uniaxial compression

N. Huber [a,*], R.N. Viswanath [a,b], N. Mameka [a], J. Markmann [a,c], J. Weißmüller [a,c]

[a] *Helmholtz-Zentrum Geesthacht, Institut für Werkstoffforschung, Werkstoffmechanik, Max-Planck-Strasse 1, 21502 Geesthacht, Germany*
[b] *Surface and Nanoscience Division, Materials Science Group, Indira Gandhi Centre for Atomic Research, Kalpakkam, India*
[c] *Institut für Werkstoffphysik und Werkstofftechnologie, Technische Universität Hamburg-Harburg, Hamburg, Germany*

Abstract

This study is motivated by discrepancies between recent experimental compression test data of nanoporus gold and the scaling laws for strength and elasticity by Gibson and Ashby. We present a systematic theoretical investigation of the relationship between microstructure and macroscopic behaviour of nanoporous metals. The microstructure is modelled by four-coordinated spherical nodes interconnected by cylindrical struts. The node positions are randomly displaced from the lattice points of a diamond lattice. We report scaling laws for Young's modulus and yield strength, which depend on the extension of nodal connections between the ligaments and the solid fraction. A comparison with the scaling laws of Gibson and Ashby revealed a significant deviation for the yield stress. The model was applied for identifying a continuum constitutive law for the solid fraction. Matching the model's predicted macroscopic stress–strain behaviour to experimental data for the flow stress at large compression strain requires the incorporation of work hardening in the constitutive law. Furthermore, the amount of disorder of the node positions is decisive in matching the model results to the experimental observations of an anomalously low stiffness and an almost complete lack of transverse plastic strain.

© 2014 The Authors. Published by Elsevier Ltd.

1. Introduction

Nanoporous metal made by dealloying takes the form of macroscopic (millimetre- or centimetre-sized) porous bodies with a solid fraction around 30% [1–3]. The material exhibits a network structure of 'ligaments' with a uniform characteristic ligament diameter that can be adjusted between 5 and 500 nm. Current research explores the use of nanoporous metal, and specifically nanoporous gold, made by dealloying as functional material with regard to catalysis [4–7], actuation [8–10] and sensing [11]. Mechanical performance is of relevance for each of these fields. It is therefore noteworthy that the strength of nanoscale objects – such as the ligaments in nanoporous gold – increases systematically with decreasing size. Nanoporous network structures made by dealloying offer themselves as suitable model systems for (i) exploring this phenomenon in experiment and (ii) implementing the high strength of individual nano-objects into a materials design strategy that yields macroscopic functional and/or structural materials which exploit the strength of nanoscale objects.

The first experimental studies of the mechanical behaviour of nanoporous gold used nanoindentation or micropillar compression. Their results, as summarized in Refs. [3,12,13], were found to agree with the Gibson–Ashby foam scaling equations [14] for the variation of strength with solid fraction and with the power-law relation between strength and structure size [15–17]. More recently, two studies using atomistic simulation have confirmed the general trends of the early experiments while suggesting corrections to the scaling law [18] and pointing towards

* Corresponding author.
E-mail address: norbert.huber@hzg.de (N. Huber).

deviations [19] between the plastic behaviour in compression and in tension. Yet, while experiments with macroscopic samples of nanoporous gold that can be deformed to large strain in compression [20,21] document the constitutive behaviour in the form of stress–strain curves that can be compared to theory and simulation, the opportunity for comparison remains yet to be exploited. This would be all the more interesting as the compression experiments expose a number of nontrivial features, most importantly a significant work hardening and, hence, uniform deformation in compression, the absence of transverse plastic strain, an apparent yield stress that is considerably below that inferred from the nano- or microscale experiments, and the accumulation of lattice defects in the form of a dislocation cell structure at large strain [20]. The most recent experiments have also shown that the flow stress of macroscopic nanoporous gold samples can be reversibly varied by up to a factor of two by simply transferring electric charge to the surfaces through electrochemical double-layer charging or reversible electrosorption, highlighting the role of the surface for the deformation behaviour [21]. Furthermore, the compression–tension anisotropy of the work hardening – which leads to instable plastic flow and brittleness in tension – can be suppressed by impregnating the pore space with a polymer [22]. This opens the way to ductilizing nanoporous gold in tension. Here, we investigate the elastic and plastic deformation behaviour of nanoporous gold in a micromechanical approach, emphasizing the comparison between the modelling and the recent experimental data for the transverse plastic behaviour, as well as the work hardening during large-strain plastic deformation under compression.

Nanoporous metals are characterized by their solid fraction $\varphi = \rho/\rho_s$, where ρ and ρ_s denote the mass densities of the porous material and of the solid skeleton phase, respectively. Although nanoporous metals typically have a solid fraction of $\varphi > 0.25$, the Gibson–Ashby model [14] for low-density cellular open foams is commonly applied to these materials [3]. In this case the scaling of the macroscopically effective values of Young's modulus, E, and yield stress, σ_y, is given in dependence of the solid fraction by

$$\frac{E}{E_s} = C_E \varphi^{n_E} \tag{1}$$

and

$$\frac{\sigma_y}{\sigma_{ys}} = C_\sigma \varphi^{n_\sigma} \tag{2}$$

respectively. In these equations E_s and σ_{ys} denote the modulus and the yield stress of the solid phase.

As summarized in Ref. [23], for bending-dominated behaviour we have $n_E = 2$ and $n_\sigma = 3/2$, while for tension-dominated behaviour $n_E = n_\sigma = 1$. As a generalization of the Gibson–Ashby model, the effect of the variation in the geometry of the skeleton on the reduced modulus was studied for different unit cell geometries [24]. Values of $1.3 < n_E < 3$ were found for the random microstructures,

indicating a more complex dependence than typically obtained for periodic cell theories.

Further work that combined the analysis based on the Gibson–Ashby model with experimental investigations on nanoporous metals suggested incorporating a Hall–Petch-type relation between the average yield strength and the average ligament diameter [13]. The impact of the surface excess elastic parameters on the effective elastic response has also been considered [25]. Motivated by the experimental findings for nanoporous metals having higher solid fractions ($\varphi \geqslant 0.4$), Liu and Antoniou [26] proposed a modified rectangular unit cell that accounts for the geometrical dimension of the additional mass at the junctions of ligaments. The scaling law for the elastic modulus required an extension by an additional geometric parameter characterizing the extension of this mass.

It was suggested very recently that the Gibson–Ashby model [14] should be modified for nanoporous metals according to their deformation mechanisms at the nanoscale [18]. The tensile behaviour and size effects of open-cell nanoporous gold were investigated using molecular dynamics (MD) simulations. Consistent with experimental results, it was found that the ultimate tensile strength of nanoporous Au depends on the average ligament diameter. In relation to Young's modulus, the scaling law was determined by calibration with the MD results. The result took the form

$$\frac{E}{E_s} = C_{E,b}\varphi^2 + C_{E,t}\varphi \tag{3}$$

where the two terms on the right side of Eq. (3) correspond to bending and tensile deformation of the ligaments, respectively, with $C_{E,b} = 0.14$ and $C_{E,t} = 0.136$. Furthermore, it was found that the yield strength in tension is dominated by axial yielding of the ligaments, for which $n_\sigma = 1$. The corresponding scaling law reduced to

$$\frac{\sigma_y}{\sigma_{ys}} = C_\sigma \varphi \tag{4}$$

The results of these studies suggest that the mechanics of nanoporous metals follow the relationships by Gibson–Ashby, where the scaling of the reduced modulus includes both bending and tension contributions, while the macroscopically effective yield stress is mainly controlled by tension.

From the literature discussed above, we can conclude that the scaling of nanoporous metals depends on the complexity of the unit cell, which also includes the degree of randomization. The loading direction (macroscopic tension or compression loading) determines if the dominating deformation in the ligaments is bending and/or tension. Most theoretical works concentrate on the elastic properties, while the literature on the scaling laws for yield stress, particularly for nanoporous metals under compression loading, is scarce.

Because large plastic deformation of nanoporous metals can only be obtained in compression tests, the experiment

and theory in the present paper focus on compressive deformation. After the experimental section, which describes the specimen preparation and testing, a section on the theoretical model follows, in which the scaling laws are derived. Motivated by electron micrographs of nanoporous gold, a new model for the microstructure is based on the unit cell of the diamond crystal lattice. The analytical model derived for such a periodic unit cell is numerically validated and then generalized for a random microstructure using finite element simulations. Finally, the resulting scaling laws are applied to identify the elastic–plastic stress–strain behaviour of the solid fraction in nanoporous gold by calibration of the numerical model to a macroscopic compression test.

2. Experimental

2.1. Specimen preparation

The preparation of nanoporous gold was based on established protocols, as described in Ref. [20]. The master alloy $Ag_{75}Au_{25}$ was arc melted based on Ag and Au (both 99.99%, Sigma Aldrich), and homogenized by a 12 h vacuum anneal at 750 °C. Wire-drawing and cutting with a wire saw yielded cylindrical samples of 1.5 mm in diameter and 2.85 mm in length. The samples were then electrochemically dealloyed in 1 M $HClO_4$ at 293 K, using a dealloying potential of 0.75 V vs. a Ag/AgCl pseudo-reference electrode in the same solution. Using ultrapure water, the samples were repeatedly rinsed and then immersed in a bath at 348 K for 12 h.

Analysis of scanning electron microscopy (SEM) images yielded a mean ligament diameter of 63 ± 6 nm from 50 individual ligaments. A representative SEM image is shown in Fig. 1. Energy-dispersive analysis of X-ray fluorescence in the scanning electron microscope reveals $\leqslant 2$ at.% Ag in the porous metal. Based on sample mass, composition and external dimensions, the solid volume fraction, φ was estimated to be $\varphi = 0.26 \pm 0.01$ for the as-prepared porous metal.

2.2. Compression testing

Compression tests on the cylindrical samples used a Zwick Z010 TN testing machine with a calibrated load cell. The strain was computed from the displacement of the load surfaces as measured by a laser speckle extensometer (Zwick laserXtens) with an object lens matched to the sample dimension. True stress and true strain were computed from the elongation by exploiting the finding of a constant cross-section [20,22]. That finding also suggests that the tests were not impaired by friction at the load surfaces. Since porous samples start to expand laterally when compressed to near full density, the compression data was evaluated only up to an upper limit of true compressive strain of 0.5.

Load/unload segments served to explore the evolution of the stiffness as the compression proceeded. These segments used exactly the same engineering strain rate as the main compression test, $\dot{\varepsilon} = 3.5 \times 10^{-4} s^{-1}$. The corresponding Young's moduli were determined by a straight line fit to the linear part of the load/unload segments. At higher strains, these segments tend to develop a considerable hysteresis. In these cases, a tangent modulus, as defined, for instance, in Ref. [27], was determined by a straight line fit of the upper half of the unloading segment.

3. Modelling

3.1. Scaling laws for a ball-and-stick model

3.1.1. Geometry and solid fraction

Micrographs of nanoporous gold (e.g. Figs. 1 and 2) show a network of ligaments connected in nodes. Depending on the node under observation, we find either three or four ligaments joining. Here we adopt the simplest
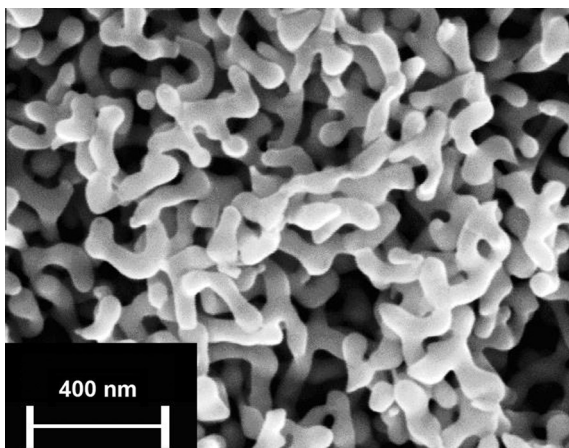

Fig. 1. Scanning electron micrograph of the surface of a nanoporous gold sample, illustrating the nanoscale network structure.
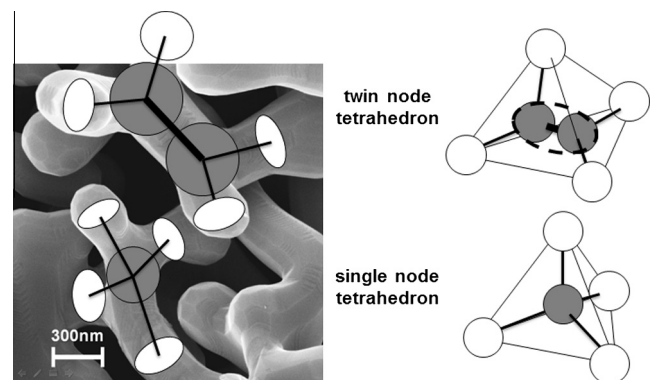

Fig. 2. Simplification of three-dimensional interconnected nanostructure to a ball-and-stick model with tetrahedrons as building blocks. The scanning electron micrograph of annealed nanoporous gold is reproduced by courtesy of Dr. H.-J. Jin, Institute of Metal Research, Shenjang.

structure based only on four-coordinated nodes as a periodic array of tetragonal cells, which are composed of beams (ligaments) and spheres (nodes connecting the ligaments). Furthermore, it is assumed that the ligaments are cylindrical.

According to Appendix A.1, our representative structure is characterized by the unit cell size, a, the node spacing, l, the ligament radius, r, and the node radius, R, with $r/R = \sqrt{2/3}$. A generalized geometry includes a geometry parameter $c_R \geqslant 1$, so that $R = rc_R\sqrt{3/2}$. For $c_R > 1$, neighbouring ligaments do not touch at the node surface and the extended spherical node smoothens the notch at the closest approach of the ligaments.

The solid fraction φ, which is defined by the described choice of the unit cell geometry, forms the basis for the model. Its calculation from the unit cell geometry is derived in Appendix A.1 and is given by Eq. (A.3) as

$$\varphi = \frac{3\sqrt{3}}{4}\pi\left(\frac{r}{l}\right)^3\left[\frac{l}{r} + \left(2c_R^2 - \frac{4}{3}\right)\sqrt{\frac{3}{2}c_R^2 - 1} - \sqrt{\frac{3}{2}}c_R^3\right] \quad (5)$$

For the common assumption of thin beams, which ignores the volume of the nodes, Eq. (5) simplifies to

$$\varphi = \frac{3\sqrt{3}}{4}\pi\left(\frac{r}{l}\right)^2 \quad (6)$$

Comparing the plots of Eqs. (5) and (6) in Fig. 3, it can be seen that the deviation is considerable. The thin-beam approximation, Eq. (6), overestimates the volume of the beams because it ignores their overlap near the junction points. From the curves of the more realistic node model, Eq. (5) and their dependence of the parameter C_R it can be seen that the nodes can occupy a significant volume fraction of the material.

The relative deviation between the respective solid fractions reaches 15% at a solid fraction of $\varphi = 0.1$ (corresponding to $r/l = 0.17$). For the nanoporous gold

Fig. 3. Dependency of the solid fraction, φ, on the geometry of the unit cell as parametrized by the ratio of ligament radius, r, over node spacing, l. Solid lines: plot of Eq. (5) valid for thick beams and extended nodes with node size parametrized by coefficient c_R (labels). Dashed line: thin beam assumption, Eq. (6).

presented in Section 2, the solid fraction is $\varphi = 0.26$ and the relative deviation is 22%.

3.1.2. Mechanical properties

The stiffness of the unit cell can be derived for the given unit cell geometry using the Euler–Bernoulli theory (see Appendix A.2, Eq. (A.4)). This yields the relationship for the macroscopically effective modulus in the form

$$\frac{E}{E_S} = c_E\left(\frac{r}{l}\right)^4, \quad c_E = \frac{9\sqrt{3}}{8}\pi \approx 6.1 \quad (7)$$

Eq. (7) holds for thin beams and negligible node size. By inserting the solid fraction given from Eq. (6), we obtain

$$\frac{E}{E_S} = \frac{2}{\pi\sqrt{3}}\varphi^2 \approx 0.37\varphi^2 = C_E\varphi^2 \quad (8)$$

The power law exponent agrees with that of the Gibson–Ashby relation [24]. By contrast, at 0.37 the value of the pre-factor C_E is only half that of Gibson and Ashby, which has a value of $C_E = 2/3$. This means that our ball-and-stick diamond lattice model is about a factor of 2 more compliant compared to the periodic models of open cell solids presented in Ref. [24].

The presence of nodes of finite extension reduces the free length of the ligaments only slightly, because the elastic strain field penetrates well into the node and therefore it will also contribute to the compliance of the unit cell. Therefore, this effect shall be ignored here. According to Appendix A.3, Eq. (A.5), the scaling law for the macroscopic yield stress for the diamond unit cell is given by

$$\frac{\sigma_y}{\sigma_{yS}} = c_{\sigma_y}\left(\frac{r}{l}\right)^3, \quad c_{\sigma_y} = \frac{3}{8}\sqrt{\frac{3}{2}}\pi \approx 1.4 \quad (9)$$

Eq. (9) does not account for the extension of the node to which the ligament is connected. However, the onset of plastic deformation occurs locally at the transition of the thin ligament to the thicker node. To account for the localized plastic yielding, a reduction of the length of the lever available for bending of the ligament by the node radius R of the form $l_b' = l_b - R$ is included. It is directly proportional the bending moment M_b and therefore also to the yield stress σ_{yS}. Accordingly, the correction of the effect of the node radius needs to be considered in the form

$$\frac{\sigma_y}{\sigma_{yS}} = c_{\sigma_y}\left(\frac{r}{l}\right)^3\left(1 - \sqrt{6}c_R\frac{r}{l}\right)^{-1}, \quad \frac{r}{l} < \frac{1}{\sqrt{6}c_R} \quad (10)$$

3.2. Finite element simulations

The analytical model presented in Section 3.1 gives a first insight into the scaling of the elastic modulus and yield stress of a nanoporous metal under the assumptions that the beams are sufficiently thin (i.e. the Euler–Bernoulli theory is valid) and that the nodes and beams are all of the same geometrical size, described by the parameters R, c_R, r and l. A generalization towards more realistic nanostructures with a solid fraction of the order of 30% is required,
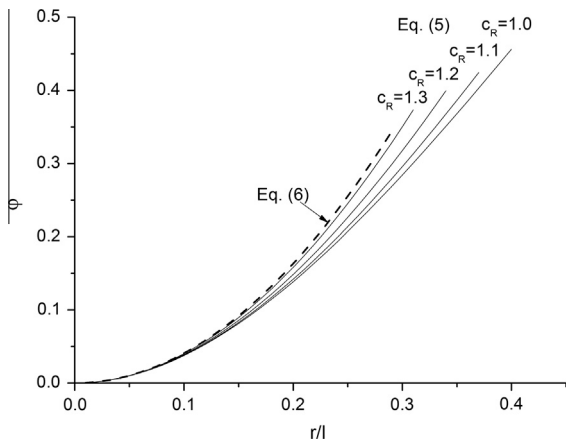
according to Figs. 1 and 3, to account for a variation of the parameter ratio r/l for individual ligaments as well as thick beams (Timoshenko beam theory), respectively. Both can be achieved by finite element simulations.

3.2.1. The finite element method (FEM) solid model

A ball-and-stick model with a face-centred cubic (fcc) diamond lattice was modelled as a solid model in ABAQUS with 257760 C3-D6 elements [28]. The unit cell size was set to unity $a = 1$ mm without restriction of generality so that, for this solid model, $l = 0.433$ mm, $r = 0.070$ mm, $R = 0.0857$ mm and $r/l = 0.162$. To avoid a sharp notch between touching ligaments, the nodes were modelled with a slightly larger node radius, leading to $c_R \approx 1.1$ and a solid fraction φ of 9.55%. The 3-D model of the building block is shown in Fig. 4a. As a consequence of $c_R > 1$, the connection between the ligaments is rounded. The appearance of the geometry in this transition area is a good approximation of the smooth surface observed in the micrograph shown in Fig. 2. Further analysis of the experiments will therefore also be based on the estimation of $c_R \approx 1.1$ (see Section 4.3).
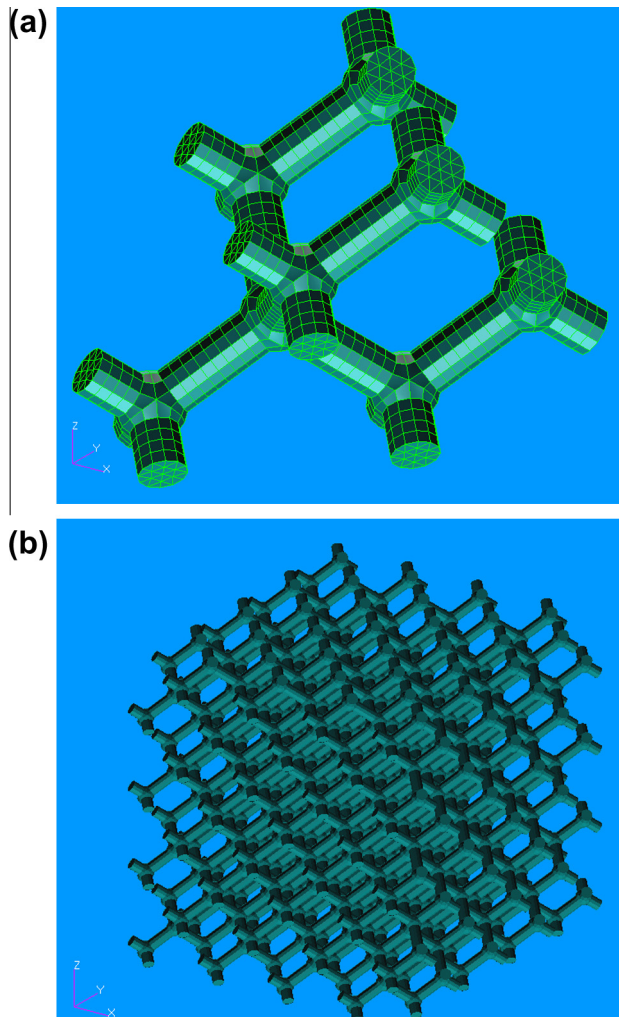
Fig. 4. Finite element meshes for the solid model: (a) building block; (b) complete model with $4 \times 4 \times 4$ unit cells.

The complete 3-D model of the representative volume element (RVE) consists of $4 \times 4 \times 4$ unit cells (see Fig. 4b). This size was chosen to reduce any possible effects of the load introduction on the top face at an acceptable computation time of 3 CPU h and 15 CPU h for elastic and elastic–plastic simulation, respectively. Symmetry conditions are applied to the nodes on the planes $x = 0$, $y = 0$ and $z = 0$. The load is applied as a homogeneous displacement of all nodes on the top side of the RVE. All nodes on the side faces are free to move, to capture the boundary conditions of the uniaxial compression experiment as described in Section 2. The material behaviour is isotropic elasticity for the determination of the macroscopic stiffness and ideal (isotropic) plasticity for the determination of the macroscopic yield stress.

The solid model serves for validation of the beam model and the assessment of the errors induced by the simplification of the 3-D structure as beams. Furthermore it allows validation of the correction of the reduced lever length by the node size as it has been included in Eq. (10).

3.2.2. FEM beam models

The finite element method provides special beam elements that contain the relevant mechanics in the element formulation and can help to efficiently simplify 3-D solid models by replacing beam-like geometries by such beam elements. Such a 3-D FEM beam model is shown in Fig. 5a. Each ligament is modelled by a sequence of 20 individual B31 beam elements [28]. The beam elements allow transverse shear strain, which leads to Timoshenko beam theory and is generally considered useful for thicker beams, whose shear flexibility may be important.

The $4 \times 4 \times 4$ unit cell RVE consists of 20,480 beam elements. By simplifying the model to beam elements, the computation time in ABAQUS is reduced by a factor of about 3500, so that an elastic simulation takes only about 4 s. It is also possible to apply large plastic deformations, leading to 0.5 CPU h computation time.

The beam model allows the dependency of the geometry parameter r/l to be studied by variation of the ligament radius through changing the element properties. Furthermore, it is possible to modify the individual ligament length by shifting each connecting node by a given random displacement. To model a more realistic interconnected structure, as suggested by Fig. 1, it is assumed that the connecting nodes are shifted randomly by amplitude A. The shift along each coordinate direction u_i is an independent random number in the interval $-A \leqslant u_i \leqslant +A$ obtained from an equal distribution in the given interval. A typical mesh with amplitude $A = 0.3a$ is shown in Fig. 5b.

4. Results and discussion

4.1. Analytical scaling laws and FEM results

The validation of the theoretical models is carried out for the regular structures ($A = 0$), assuming a value of
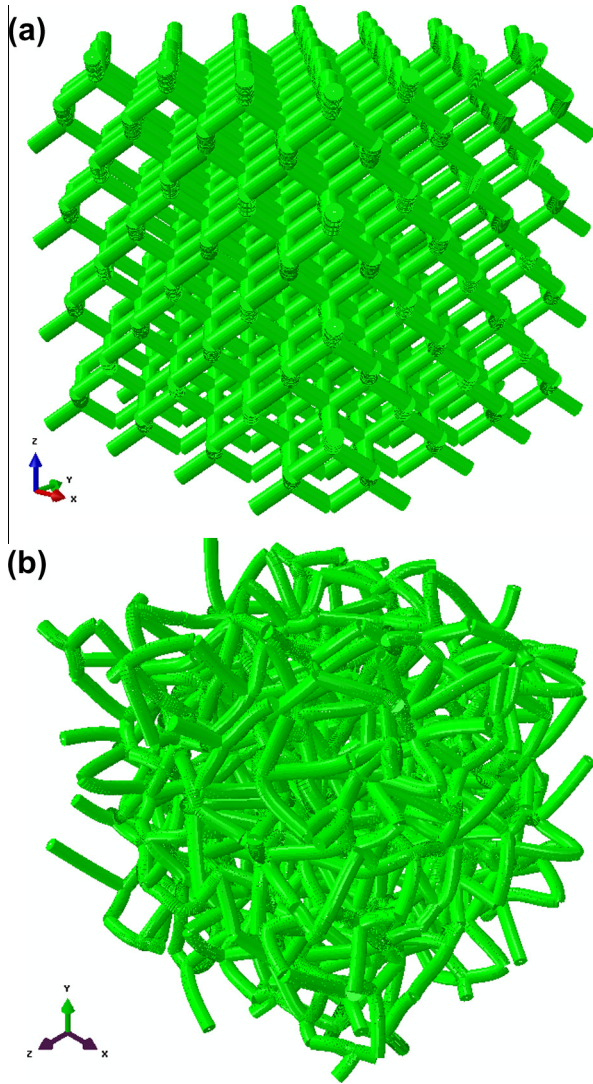
Fig. 5. Finite element meshes for the beam model: (a) periodic RVE generated from 64 unit cells; (b) RVE produced by random shift of connecting nodes by amplitude $A = 0.3a$.
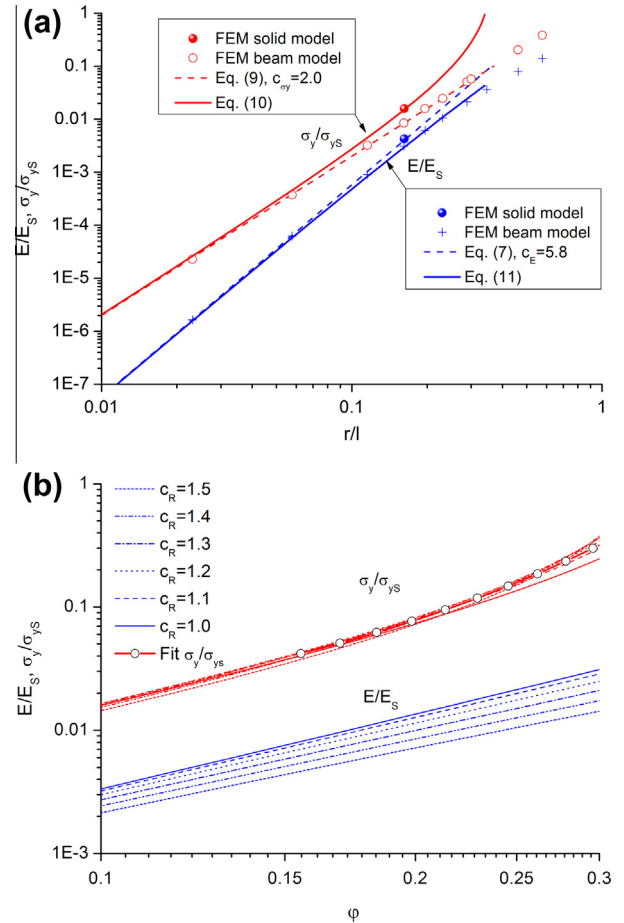

Fig. 6. Scaling laws for modulus and yield stress: (a) validation of analytical models by FEM simulations ($c_R = 1.1$); (b) representation in dependency of the solid fraction and the geometry parameter c_R.

$c_R = 1.1$ as defined in the solid model. Fig. 6a shows a summary of all of the results for both cases: elasticity and plasticity. For thin beams, the slope of both scaling laws, Eqs. (7) and (9), is confirmed by the FEM beam model. The constant c_E determined from the simulations is $c_E = 5.8$, which is 5% below the theoretical value given in Eq. (7). For the yield stress, the constant is determined with $c_{\sigma_y} = 2.0$, showing a deviation of 39% with regard to Eq. (9). The solid model shows a stiffness increase of 38% compared to the beam model, while the yield strength is increased by 87%. Thus, for this specific geometry, the effect of the reduced lever is about twice as significant for plastic deformation, confirming the assumptions that lead to the correction in the form of Eq. (10). Viewing the von Mises stress distribution in the solid model, it can be confirmed that onset of plastic yield occurs at the end of the ligaments where they are connected to the node.

The effect of the Timoshenko beam theory, which is included in the FEM beam model, becomes visible for

$r/l > 0.1$, corresponding to a solid fraction of only $\varphi = 3.6\%$. Above this value a correct prediction of the elastic scaling law requires a modification of the scaling law, Eq. (7). A better fit to the finite element results can be achieved by a change of the power in the scaling law from 4 to 2 when r/l is approaching a large value, for example of the form

$$\frac{E}{E_S} = c_E \left(\frac{r}{l}\right)^4 \left(1 + \frac{r}{l}\right)^{-4} \left(1 + \frac{r}{l}\right)^2, \quad c_E = 5.8 \qquad (11)$$

A transfer of the scaling laws for the yield strength and the modulus, as provided by Eqs. (10) and (11), into a representation of the solid fraction using Eq. (5) is given in Fig. 6b for the relevant range of the solid fraction in experiments. While, for the plots in Fig. 6a, the parameter $c_R = 1.1$ is fixed according to the geometry of the finite element model, it is varied from 1.0 to 1.5 in Fig. 6b. This delivers an insight into the effect of uncertainties in the estimation of c_R on the predicted mechanical properties. As the effect of reduced lever length has been ignored in the scaling law for the modulus, given in Eqs. (7) and (11), the scaling law is simply shifted right with increasing c_R through its effect on the solid fraction following Eq. (5).

All curves remain straight lines in the log–log plot of Fig. 6b, which is confirmed by the correlation coefficient for the linear fits by Eq. (1), as given in Table 1. The constants C_E and n_E are also given in Table 1 in dependence of c_R.

In contrast to the stiffness, the yield strength has been corrected for a reduction of lever length through the node size according to Eq. (10). Interestingly, with increasing c_R, the resulting strength increase nearly compensates for the increase in the solid fraction, so that all presented curves for $c_R > 1.0$ lie within a very thin band, which is, however, nonlinear. The fit of the scaling law for the macroscopic yield stress, displayed in Fig. 6b, is an exponential function of the form

$$\frac{\sigma_y}{\sigma_{ys}} \approx \mathrm{b}e^{c\varphi} \qquad (12)$$

for which the fit constants $b = 4.74 \times 10^{-3}$ and $c = 14.02$ are determined for solid fractions φ from 0.15 to 0.37. This exponential type behaviour deviates significantly from the Gibson–Ashby model.

4.2. Effect of randomized nodal positions

4.2.1. Effect on deformation behaviour

A study of the effect for the parameter $A = 0 - 0.5$ was carried out with the following material parameters for the solid fraction: $E_s = 81$ GPa, $v = 0.42$. For the elastic–plastic behaviour, the yield stress is set to $\sigma_y = 500$ MPa (isotropic plasticity, no work hardening). The geometry parameters are again $a = 1$ mm, $l = 0.433$ mm, $r = 0.07$ mm, and $r/l = 0.162$.

The simulation results for the force–displacement behaviour are presented in Fig. 7. The random shift of the nodal positions through the parameter A significantly influences the deformation behaviour of the RVE in stiffness, seen in the initial slope of the curves, as well as in strength, visible as a peak stress. The comparison between the solid model and the beam model is also included in this plot, but only for the case of elastic deformation and $A = 0$. It can be seen that the effect of randomized nodal positions is much larger than the deviation between the beam model and the solid model. The drastic gain in computation speed using the beam model for parametric studies justifies the comparably small error that is induced by ignoring the effect of the nodes for these studies.

Table 1
Parameters for the Gibson–Ashby scaling law for Young's modulus, as given by Eq. (3) in dependence of geometry parameter c_R.

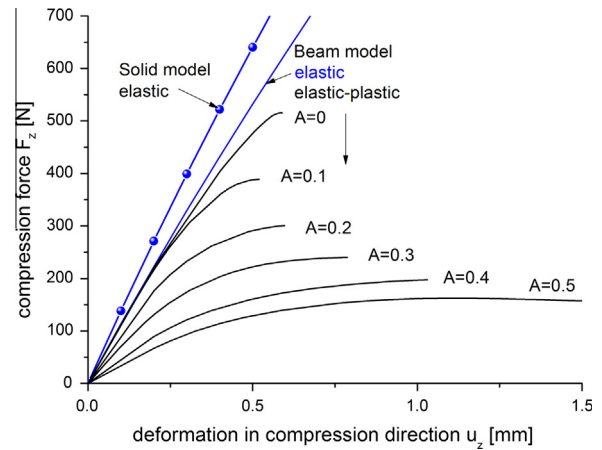| c_R	C_E	n_E	Correlation coefficient
1.0	0.344	2.01	0.99998
1.1	0.309	1.98	1.00000
1.2	0.257	1.93	0.99999
1.3	0.203	1.88	0.99994
1.4	0.158	1.82	0.99986
1.5	0.121	1.76	0.99977

Fig. 7. Effect of the random shift of nodal positions on the force–displacement behaviour under uniaxial compression.

For the same simulations, Fig. 8 shows the lateral extension of the RVE vs. the displacement in the compression direction. It is striking how strong the lateral extension decreases with increasing amplitude A. For larger values of A it is even possible to produce negative lateral extensions after some deformation, i.e. the cross-section of the material is predicted to shrink during the ongoing compression. From these results it can be concluded that, during uniaxial compression, nanoporous metals with a randomized structure should show only a small positive extension or even shrinkage in the lateral direction.

4.2.2. Effect on modulus

Fig. 9a and b present the predicted effect of the parameter A on the modulus as a function of the ratio r/l and φ, respectively. It can be seen that the reduction of the modulus is more pronounced for thin beams. The transition corresponds to the transition from an Euler–Bernoulli beam to a Timoshenko beam. The numerical results
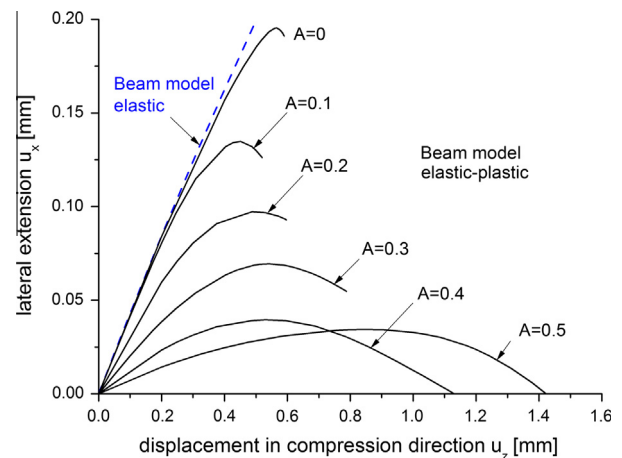

Fig. 8. Effect of the random shift of nodal positions, as parametrized by the displacement parameter A, on the lateral displacement of the side wall surface nodes during uniaxial compression of the RVE. The initial dimensions of the RVE are $4 \times 4 \times 4$ mm³.

(symbols) can be represented by a fit function as given by Eqs. (13)–(16) with the fit parameters given in Table 2, represented by thin dashed curves in Fig. 9a. Error bars are not shown because the standard deviation from 10 different random RVE realizations result in an average standard deviation of only 2%.

$$\frac{E(A)}{E(A=0)} = A_1(A) + [A_2(A) - A_1(A)][1 + 10^{(0.4-r/l)Ap(A)}]^{-1} \quad (13)$$

$$A_1(A) = 1 + a_{11}A + a_{12}A^2 + a_{13}A^3 \quad (14)$$

$$A_2(A) = 1 + a_{21}A + a_{22}A^2 + a_{23}A^3 \quad (15)$$

$$A_p(A) = a_{p1} + a_{p2}e^{-(A/a_{p3})^2} \quad (16)$$

Combining Eqs. (5), (11), (13), (14), (15), and (16), it is now possible to study the effect of randomization on the Gibson–Ashby equations. For each value of r/l, the solid fraction φ and the values for $C_E = (E(A)/E_S)\varphi^{-2}$ are calculated for $c_R = 1.0$. The results for C_E in dependence of φ, as plotted in Fig. 10, show that there is only a slight increase in C_E with increasing φ. Our numerical studies thus suggest that the variation of the macroscopic Young's modulus

Table 2
Parameters of the fit function $E(A)/E(A = 0)$, Eqs. (13)–(16).

Eq. (14)	$a_{11} = -0.04541$	$a_{12} = -6.8215$	$a_{13} = 5.9489$
Eq. (15)	$a_{21} = 0.1219$	$a_{22} = -4.6652$	$a_{23} = 4.7882$
Eq. (16)	$a_{p1} = 1.8261$	$a_{p2} = 2.9500$	$a_{p3} = 0.2412$

with the solid fraction is approximated well by Eq. (1) also for randomized nodal positions. The dependence of the power n_E on c_R is given in Table 1; the corresponding value for C_E in dependence of the solid fraction φ can be taken from Fig. 10.

4.2.3. Effect on yield stress

The influence of the parameter A on the strength of the RVE as a function of the ratio r/l and φ is presented in Fig. 11a and b. Error bars are also not shown in this case because the average standard deviation from 10 different random RVE realizations was only 3%.

We observe that local yielding will set in very early in one of the ligaments of the randomized structure. We therefore focus on the peak stress, as a parameter that is more representative of the macroscopic behaviour than the stress at the first yield event. Within the range of $0.01 \leqslant r/l \leqslant 1$ the dependence on the parameter A can be described by the single fit function

$$\sigma_y(A)/\sigma_y(A=0) = 1 - A\left[1.127 + 0.03344\left(\frac{r}{l}\right)^{-0.7269}\right]. \quad (17)$$

Compared to the sensitivity of $E(A)/E(A = 0)$ on φ for values of $\varphi > 0.1$, as shown in Fig. 9b, the sensitivity of the yield stress $\sigma_y(A)/\sigma_y(A = 0)$ is rather small (see Fig. 11b).

4.3. Experimental results and analysis in terms of the model

Fig. 12 shows experimental results of a compression test on nanoporous gold. The graph of true stress vs. true strain
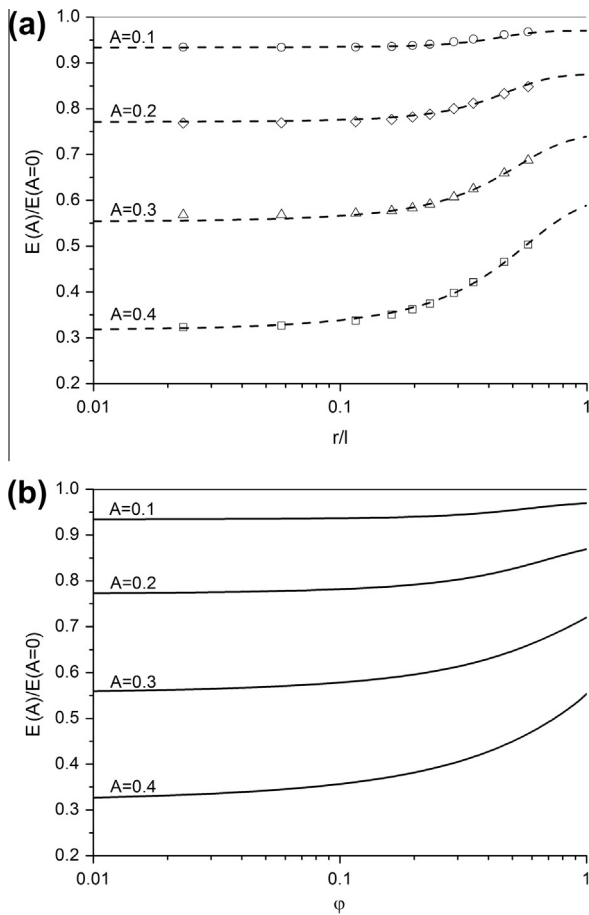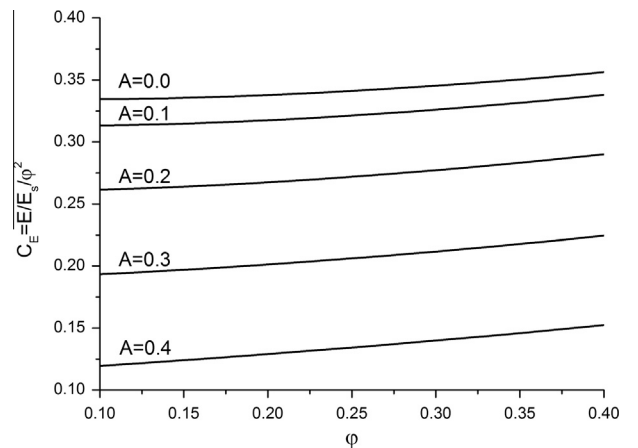
Fig. 9. Effect of random nodal position on the modulus in dependence of random amplitude A: (a) markers correspond to numerical results from the FEM beam model, dashed curves represent the fit function Eqs. (13)–(16) as a function of r/l; (b) plot of Eqs. (13)–(16) as a function of the solid fraction φ, calculated from Eq. (5) using $c_R = 1$.

Fig. 10. Constant C_E for scaling law of Young's modulus according to Eq. (1) plotted against the solid fraction φ and parametrized by the random node shift amplitude A.
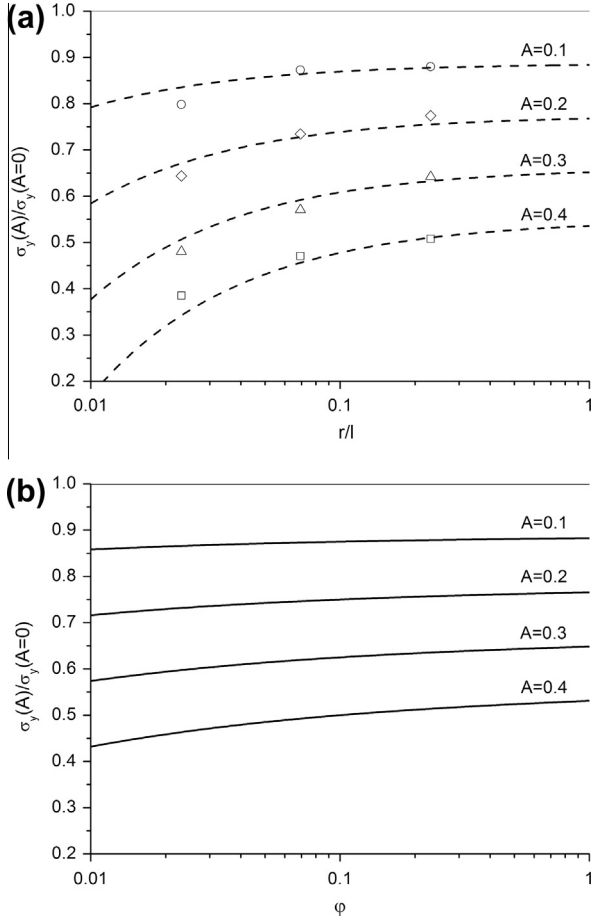
(a)

(b)

Fig. 11. Effect of random nodal position on the yield stress in dependence of random amplitude A: (a) markers correspond to numerical results from the FEM beam model, thin dashed curves represent the fit function Eq. (17); (b) plot of Eq. (17) as a function of the solid fraction φ, calculated from Eq. (5) using $c_R = 1$.
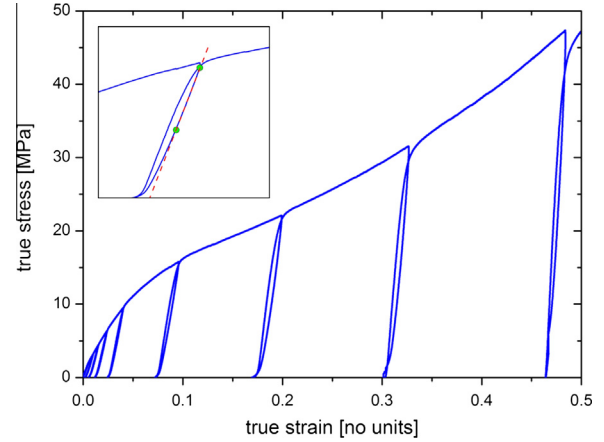

Fig. 12. Results of experimental test plotted as true stress vs. true strain. The continuous increase in load is interrupted by unloading/loading segments that serve to separate elastic and plastic deformation. Inset: details of the unload/load segment, showing the determination of modulus by linear fit of the part of the unloading curve between the intersection point between the unloading and the following loading curve, and the point where the load is half of the stress at the begin of the unloading step.

is highly consistent with previous results [20–22]. However, the data goes beyond previous reports in showing not only the envelope curve of stress vs. strain during continuously increasing deformation, but also intermediate load/unload segments, from which the elastic part of the deformation can be identified. The observation of residual strain after unloading even from quite a small stress (<3 MPa) indicates early plastic deformation. This is similar to micro-plasticity, and it is consistent with the early local yielding events in individual ligaments that were observed in the simulation. In fact, the envelope curve of stress vs. strain is rounded off to the extent that features that would allow the identification of a yield stress are entirely lacking.

In the context of the modeling results for the transverse plastic flow (see above), it is significant that no change in the cross-section of the sample was observed throughout the compression experiment. This absence of transverse plastic strain is again in agreement with previous observations reported in the literature [20–22]. We now turn to a comparison between model and experiment, starting out with basic values of the parameters. In view of the comparatively large ligament size, we ignore excess elasticity and

choose bulk values of (polycrystalline, isotropic) gold for the elastic parameters of the solid phase. Thus, Young's modulus is taken as $E_s = 81$ GPa and Poisson's ratio is set to $\nu = 0.42$. Furthermore, we adopt the experimental value for the solid fraction as $\varphi = 0.26$ (see Section 2.1). With $c_R = 1.1$, Eq. (5) can be solved numerically, yielding the ratio of ligament radius to node spacing as $r/l = 0.28$. Guided by the simulation results of Fig. 8, $A \geqslant 0.3$ was assumed as the lower bound for the randomized node shift in order to reproduce the absence of transverse plastic flow. The following sections present simulation results that were obtained with these parameters.

4.3.1. Stress–strain behaviour

For a direct comparison of the predicted macroscopic stress–strain behaviour of the RVE with the experimental result, it is necessary to transform the finite element data in such a way that the effect of the reduced length of the lever is included in the simulation of the stress–strain behaviour. This is possible by a modification of the ratio r/l according to Eq. (10), which can be rearranged as

$$\frac{\sigma_y}{\sigma_{yS}} = c_{\sigma_y} \left(\frac{r}{l}\right)^3 \left(1 - \sqrt{6}c_R \frac{r}{l}\right)^{-1} = c_{\sigma_y} \left(\frac{r^*}{l}\right)^3 \quad (18)$$

with

$$r^* = r \left(1 - \sqrt{6}c_R \frac{r}{l}\right)^{-1/3} \quad (19)$$

This means that the shorter ligaments in the 3-D solid require an extension of the ligament radius in the FEM beam model according to Eq. (19) to achieve the same ratio σ_y/σ_{yS} in the predicted response of the RVE. In our case, an increase in the ligament radius by a factor $r^*/r = 1.6$ is determined from Eq. (19). The following simulations are carried out with a ligament radius of $r^* = 0.194$ mm and a unit cell size $a = 1$ mm.

The fitting process started from an elastic–ideal plastic material law. A first iteration matched the elastic–plastic transition by a macroscopic yield stress of $\sigma_y = 6.2$ MPa. From the scaling law for the yield stress, Eq. (10), we obtain $\sigma_y(A=0)/\sigma_{yS} = 1.79 \times 10^{-1}$ and the ligament yield stress σ_{yS} can be calculated from Eq. (17) in dependence of the parameter A (see Table 3). However, the continuous increase in strength with increasing plastic deformation cannot be captured with ideal plasticity. Therefore, a linear isotropic hardening has been added as the simplest possible extension of the material model. The hardening behaviour is defined by the work hardening rate $\gamma = d\sigma/d\varepsilon_p$, where σ is the true stress and ε_p is the true plastic strain. From Table 3 it can be seen that only for $A = 0.5$ a small correction of the yield stress $\sigma_{yS}(Fit)$ by 7% was required to obtain a fit with the same stress level as the curves for $A = 0.3$ and 0.4.

The true stress–true plastic strain results of the fitting procedure are shown in Fig. 13, together with the experimental data. It is seen that the model predicts a soft transition from elastic to elastic–plastic deformation. However, the extended elastic–plastic transition of the experiment is not well reproduced, though the model does exhibit an apparent macroscopic yield point, which appears to be at about 10 MPa. The agreement between experiment and simulations is best for strains between 5% and 15%. Beyond 15% strain, the experimental graph acquires a stronger upward curvature, as can be seen from Fig. 12. This effect cannot be reproduced by the beam model. Using $A = 0.4$ (as motivated by the discussion of the elastic behaviour; see below) along with the parameters of Table 3, the local yield stress of the ligaments is identified as $\sigma_{yS} = 67$ MPa and the local work hardening rate is $\gamma = 814$ MPa.

4.3.2. Modulus

Fig. 14 shows the results for Young's modulus. The data is plotted vs. the solid fraction, which increases during compression because of the lack of transverse plastic strain. The axis scales are log–log, so that the Gibson–Ashby prediction of Eq. (8) (with $C_E = 2/3$) shows up as a straight line of slope 2. It can be seen that the experimental modulus values start out extremely low. The plastic compression first brings a rapid increase in the modulus, which slows down after the value has doubled to ~600 MPa. Irrespective of that stiffening, the sample at any state of deformation remains significantly more compliant than predicted by the Gibson–Ashby law. In fact, at ~320 MPa, the modulus value after the unload at 0.2% plastic strain is more
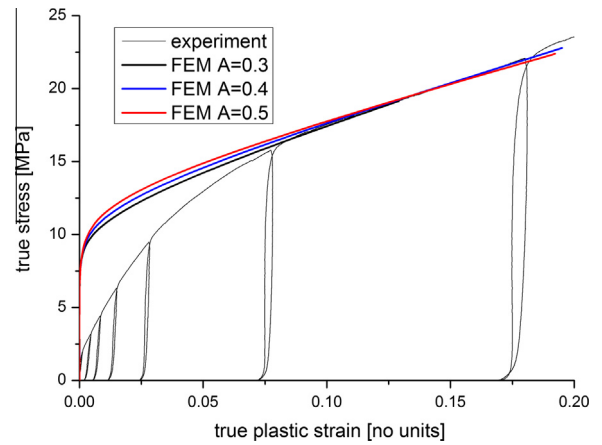

Fig. 13. Graphs of true stress vs. true plastic strain, comparing the experimental data for nanoporous gold (black solid line) to the FEM beam model (coloured lines labelled in the graph). Model results were matched to experimental data by using the work hardening rate as a free fit parameter. The values of A (indicated by labels) ranged from 0.3 to 0.5. (For interpretation of the references to colour in this figure legend, the reader is referred to the web version of this article.)
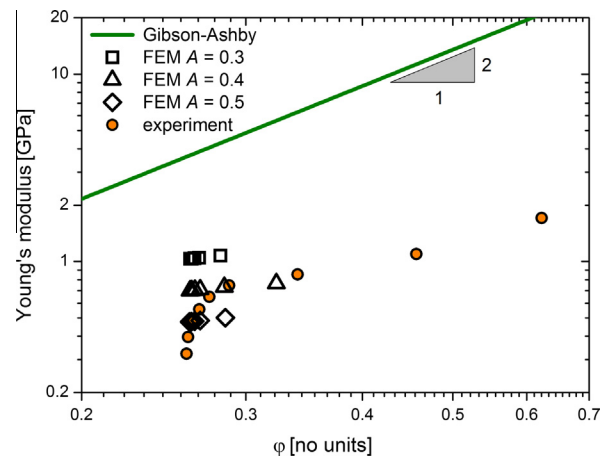

Fig. 14. Comparison of Young's modulus determined by analysis of the unloading/reloading cycles from the experiment and from the FEM simulations. The increase in relative density φ was determined via the decrease in volume described by the corresponding plastic true strain during axial compression assuming a constant cross-sectional area. The green curve represents the behaviour of an ideal isotropic open foam according to Gibson and Ashby, with $E_S = 81$ GPa, $n_E = 2$ and $C_E = 2/3$.

than tenfold less than the Gibson–Ashby prediction of ~3600 MPa.

Fig. 14 also compares the results for Young's modulus determined from the unloading segments in the experiment

Table 3
Yield stress as derived from scaling law and hardening rule as determined from the fit of the experimental behaviour for $0.3 \leqslant A \leqslant 0.5$.

A	Scaling law, Eqs. (10) and (17)			Fitted FEM beam model	
	$\frac{\sigma_y(A)}{\sigma_y(0)}$	$\frac{\sigma_y(A)}{\sigma_{yS}}$	σ_{yS} (MPa)	$\sigma_{yS}(Fit)$ (MPa)	γ (MPa)
0.3	0.64	1.14×10^{-1}	55	55	542
0.4	0.52	9.22×10^{-2}	67	67	814
0.5	0.39	7.05×10^{-2}	88	82	1061

to those from the FEM simulations using the parameters of Table 3. Contrary to the simulations in the previous subsection, the present ones kept the ratio of the ligament radius to node spacing unchanged at $r/l = 0.28$. This reflects the discussions in Sections 3.1.2 and 4.1, which concluded that the effect of the nodes on the stiffness should be ignored.

Comparing the simulation results to the experimental data, one sees that the initial steep increase in stiffness of the experiment has no analogue in the simulation. However, it is readily perceived that the unexpectedly low stiffness of the experiment is in excellent agreement with the model results. The strong impact of the random node displacement parameter A on the stiffness in the simulation is noteworthy. After the initial deformation, simulation and experiment are actually in good agreement for $A = 0.4$. This finding is also consistent with the independent conclusion on the value of A obtained when matching the transverse plastic strain.

5. Conclusions

This work presents a systematic theoretical investigation of the relationship between the microstructure and the macroscopic behaviour of the network-like nanoporous metal microstructures that are created by dealloying. The model approximates the material's microstructure by a diamond lattice with spherical nodes in randomized positions. Cylindrical beams, representing the nanosized ligaments, are connected in the nodes. We have recorded experimental compression test data for the elastic and plastic response of nanoporous gold, and compare the results to the model.

Major outcomes of this work are modified scaling laws for the modulus and yield strength, which account for the extension of the nodal volume. The study focuses on macroscopic deformation under compression, which allows it to connect to experimental data for tests up to large compression strain. As a consequence of this deformation mode, the ligaments deform mainly through bending, while contributions through deformation in the direction of the ligament axis, typically found for tension loading of a nanoporous material, are small.

The scaling law for the elastic modulus was found to agree with Gibson and Ashby as far as the power law exponent is concerned. By contrast, the pre-factor of our model is reduced. For the ordered diamond lattice, the reduction is by a factor of two. More importantly, a significant deviation was found for the macroscopic yield stress. This is mainly caused by a shortening of the ligaments due to the volume occupied by the connecting nodes. Plastic yielding occurs in our simulation locally at the transition from the ligament to the node. This is consistent with high-resolution transmission electron microscopy on deformed nanoporous gold specimens [29], which show lattice defects generated in the nodes. Longer ligaments create more torque and are thereby more efficient at initiating yielding. Therefore, the length of the ligaments controls the macroscopic yield

strength. In the case of the material's stiffness, such effects are much less pronounced because the elastic strains are expected to distribute along the whole ligaments and well into the nodes.

When randomizing the nodal positions, we find that the experimentally observed absence of lateral expansion under compression loading can be reproduced. A systematic study of the variation of the randomization amplitude was carried out and fit functions were provided that allow for corrections of the modulus and yield strength as functions of this amplitude. It was shown that its value can be calibrated from the unloading stiffness measured from unloading segments in compression experiments.

The compression experiments on nanoporous gold reveal several remarkable features, specifically the absence of transverse plastic strain, an extended elastic–plastic transition region, pronounced work hardening and compliance values that exhibit a remarkable strong initial response to densification and abnormally high values throughout the entire test.

The pronounced work hardening of nanoporous metal in compression had been reported in several earlier publications [20–22]. In the spirit of the scaling relation between the solid fraction and strength, the densification during compression is in itself a reason for strong work hardening. However, our simulations show that densification alone is not sufficient to explain the experimental observation. Instead, work hardening needs to be introduced into the constitutive law for the flow behaviour of the ligaments in order to match the experimental observation. Constitutive work hardening over extended regions of plastic strain is not compatible with the notion – prompted by similar statements in relation to the high strength of nanopillars [30] – that dislocation starvation could govern the plastic behaviour of the nanoscale ligaments. Instead, our observation testifies to dislocation accumulation and increasing dislocation–dislocation interaction as the deformation proceeds, even at the very small structure size of our experiment. This conclusion is fully consistent with the observation of the formation of a mosaic structure and, hence, the formation of dislocation cell structures in nanoporous gold during compression in Ref. [20].

The absence of transverse plastic strain is a characteristic signature of nanoporous gold compression [20–22]. This feature emerges naturally from the simulation when the array of nodal points is disordered. The observation highlights that the deformation behaviour of nanoporous gold can only be understood if a considerable amount of structural disorder is assumed.

It appears natural to also invoke structural disorder as the origin of the extended elastic plastic transition. Similar features – though much less extended on the stress and strain scales – have been observed in nanocrystalline metals [31], and can be linked to distributions of yield points [32]. In our simulation, the heterogeneity in the nodal point spacing and the local "bond angles" between adjacent ligaments introduces such a distribution. However, the failure

of the model to reproduce the extended elastic plastic transition of the experiment indicates that nanoporous gold exhibits additional features that lead to a distribution of local yield points. Such features may be the variation in ligament diameter as well as the intrinsic heterogeneous stress distribution that arises (i) from the action of the capillary forces (namely, the surface stress) along with the action of the external load and (ii) from the collapse of some ligaments during the synthesis, as suggested from experimental volume shrinkage data [33] and from molecular dynamics simulations [34].

It is easily conceivable that this structural heterogeneity and its consequence, the extended elastic plastic transition region, are also at the origin of the initial compliance increase during the early stages of deformation. The weakest regions, and the microstructure, which yield first are likely also the most compliant ones. If these regions yield, they densify and thereby stiffen. This process will actually make the compressed structure more homogeneous, both plastically and elastically. The trend towards a more homogeneous material during the compression experiments may explain why the match between the experiment and the model structure is improved at larger compressive strains. Similar to the compressed nanoporous gold, the model features local disorder, but is otherwise highly homogeneous.

The abnormal compliance found in the experiments is highly remarkable, with the initial Young's modulus of nanoporous gold a factor of 10 below the Gibson–Ashby prediction and thus more than 200-fold below the Young's modulus of massive gold. Previous nanoindentation tests had indicated a similar trend [35]. The simulation data provide a good match to the experimental elasticity data, at least after the initial yielding and homogenization of the material in the experiment. This confirms the validity of the experimental observation, and the model findings indicate that structural disorder in the network has a strong impact on the effective elastic response. The variation of the modulus with density during compression is less than the φ^2 behaviour that might be expected in view of the scaling for modulus vs. density for isotropic porous solids. It appears natural to attribute the high compliance during densification to the texture of the ligaments: as the ligament orientation distribution changes from isotropic to transversal isotropic during macroscopic compression, more and more elastic strain is accommodated by the softer bending mode as opposed to local axial compression.

In conclusion, with this work, a coupled experimental–theoretical approach has been provided that forms a sound basis for the determination of the mechanical behaviour, representing the level of nanosized ligaments.

Acknowledgements

Appendix A. Micromechanics of the diamond unit cell

A.1. Solid fraction

A view of the diamond unit cell in the $\langle 1\,1\,0 \rangle$ direction is shown in Fig. A.1a and the detail of a ligament connecting two nodes is given in Fig. A.1b. In these figures, a is the unit cell size, $d = a\sqrt{2}$ is the diagonal of the base plane, and the node spacing, l, can be determined from the ratio l/a, which is

$$\frac{l}{a} = \frac{\sqrt{3}}{4} \tag{A.1}$$

The detail in Fig. A.1b defines the projection of the node spacing l onto the base plane diagonal with length l_d. Further geometric dimensions are the ligament radius r and the node radius R, which is split into the two lengths, h_1 and h_2, by the intersection of the ligament surface and the node surface. When the geometry of the ligaments and nodes are assumed in such a way that two ligaments touch at the surface of a node, the ratio of ligament radius to node radius is given by $r/R = \sqrt{2/3}$.

A more generalized geometry allowing node radii $R > r\sqrt{3/2}$ can be considered by adding a geometry
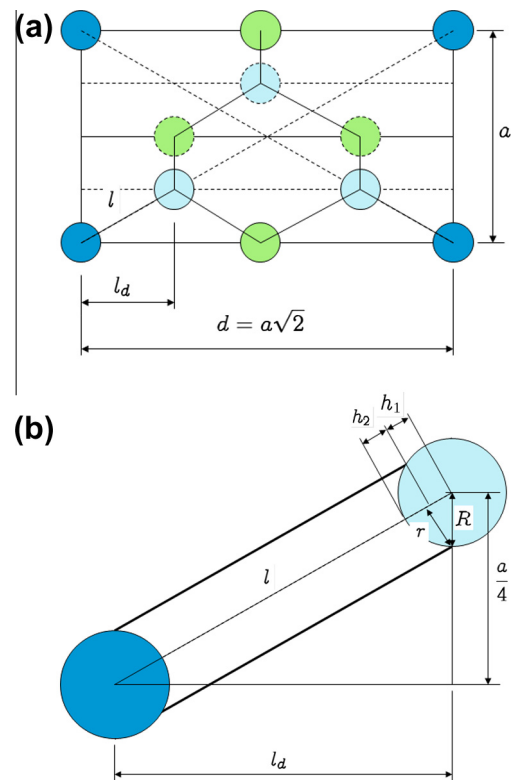

Fig. A.1. Schematic view of the fcc diamond unit cell in the $\langle 1\,1\,0 \rangle$ direction; nodes marked with a dashed contour represent two nodes located behind each other. (a) unit cell; (b) detail of a half ligament.

parameter $c_R \geqslant 1$, so that $R = r c_R \sqrt{3/2}$. For $c_R > 1$, the ligaments do not touch each other at the node surface and the extended spherical node forms a facet-like transition between the two ligaments.

The filled volume of a single tetrahedron is composed of the volumes of the spherical nodes $V_N = 4/3 \cdot \pi R^3$ and the cylindrical ligaments $V_L = \pi r^2 (l - 2R)$. Both share a volume of a spherical cap $V_C = \pi/3 \cdot h_2^2 (3R - h_2)$, where $h_1 = R/\sqrt{3}$ and $h_2 = R - h_1 = (1 - 1/\sqrt{3})R$. The smallest building block of a tetrahedron is a half ligament attached to a quarter node, sharing one spherical cap. The volume of such a building block (BB) is calculated as:

$$V_{BB} = \frac{1}{4}V_N + \frac{1}{2}V_L - V_C$$
$$= \frac{\pi}{3}R^3 + \frac{\pi}{2}r^2(l - 2R) - \frac{\pi}{3}h_2^2(3R - h_2)$$

After inserting h_2 and R in dependence of r, we obtain, after some rearrangement,

$$V_{BB} = \frac{\pi}{2}r^3 \left(\frac{l}{r} + \frac{\sqrt{2}}{3} - \sqrt{\frac{3}{2}} \right)$$

The volume of one tetrahedron $V_T = 8V_{BB}$ and the volume of the unit cell V_{UC} is composed of four tetrahedrons, so that $V_{UC} = 32V_{BB}$, or

$$V_{UC} = 16\pi r^3 \left(\frac{l}{r} + \frac{\sqrt{2}}{3} - \sqrt{\frac{3}{2}} \right)$$

Normalizing V_{UC} with the volume of the unit cell $V_a = a^3$ and replacing a through l using Eq. (A.1), the solid fraction of the unit cell is finally given by

$$\varphi = \frac{V_{UC}}{V_a} = \frac{3\sqrt{3}}{4}\pi \left(\frac{r}{l}\right)^3 \left(\frac{l}{r} + \frac{\sqrt{2}}{3} - \sqrt{\frac{3}{2}} \right) \qquad (A.2)$$

In the case where the node radius is allowed to take more general values $c_R \geqslant 1$, we obtain for the volume of the building block

$$V_{BB} = \frac{\pi}{2}r^3 \left[\frac{l}{r} + \left(2c_R^2 - \frac{4}{3}\right)\sqrt{\frac{3}{2}c_R^2 - 1} - \sqrt{\frac{3}{2}}c_R^3 \right]$$

and accordingly we have for the solid fraction of the unit cell

$$\varphi = \frac{3\sqrt{3}}{4}\pi \left(\frac{r}{l}\right)^3 \left[\frac{l}{r} + \left(2c_R^2 - \frac{4}{3}\right)\sqrt{\frac{3}{2}c_R^2 - 1} - \sqrt{\frac{3}{2}}c_R^3 \right] \quad (A.3)$$

A.2. Stiffness and modulus

For the calculation of the stiffness under a compression force F, which is applied to the top face of the unit cell, it is assumed that bending of the ligaments is the major deformation mechanism, as sketched in Fig. A.2. In this case, the detail shown in Fig. A.2b includes all relevant information, which is needed for the stiffness calculation. Although

the ligaments cannot be assumed to be thin, an Euler–Bernoulli beam theory is applied here so that a simple closed form solution can be derived.

According to Fig. A.2, the half beam of length $l_b = l/2$ is loaded normal to its beam axis by a bending force $F_b = F_v \cdot \cos\alpha$, with $\cos\alpha = \sqrt{2/3}$ and $F_v = F/4$ denoting the vertical force applied onto each node of the tetrahedron. From Euler–Bernoulli beam theory, the deflection of the beam is given as $W_b = F_b l_b^3/(3EI)$, where E_S is the Young's modulus of the solid phase, l_b is the lever and $I = (\pi/4)r^4$ is the moment of inertia. When the extension of the node is ignored in the first step, the vertical component of the displacement w_v is given by

$$w_v = \frac{F_v l^3}{9\pi E r^4}$$

The resulting vertical spring stiffness of a half beam segment is

$$S_{hb} = \frac{F_v}{w_v} = 9\pi E_S \frac{r^4}{l^3}$$

Assuming that all beams in the unit cell have the same stiffness, the resulting unit cell stiffness is obtained from

$$S_{UC} = \frac{S_{hb}}{2} = \frac{9}{2}\pi E_S \frac{r^4}{l^3}$$

On the other hand, the unit cell stiffness is also defined from the homogenized modulus of the nanoporous material, which is calculated from $E = S_{UC}/a$ so that we obtain, after again inserting a as function of l,

$$\frac{E}{E_S} = c_E \left(\frac{r}{l}\right)^4, \quad c_E = \frac{9\sqrt{3}}{8}\pi \approx 6.1 \qquad (A.4)$$
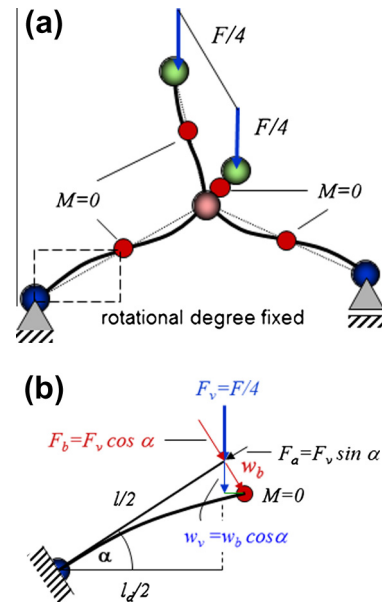

Fig. A.2. Deformation of the tetragonal building block under compression loading: (a) tetrahedron building block under applied load; (b) details of the area marked as a dashed box in (a) showing the deformation of a half ligament.

A.3. Yield stress

The assumed deformation shown in Fig. A.2 implies that plastic yield will start at the outer fibre of the ligament, exactly at the point where it is connecting to the node. The bending stress in this point as given from beam theory is $\sigma_b = M_b/W$, where $W = \pi r^3/4$ is the section modulus for the circular ligament cross-section. As shown in the detail of Fig. A.2b, the bending moment is

$$M_b = F_b l_b = \sqrt{\frac{2}{3}} \frac{F_v l}{2}$$

The bending stress reaches the yield stress of the solid phase $\sigma_b = \sigma_{yS}$ at the same time as the macroscopically plastic yield occurs so that

$$\sigma_{yS} = \frac{1}{\sqrt{6}} \frac{Fl}{\pi r^3}, \text{ as well as } \sigma_y = \frac{F}{A} = \frac{3F}{16 l^2}$$

By dividing the macroscopic yield stress σ_y by the yield stress of the solid phase σ_{yS}, we finally obtain the scaling law for the yield stress in the form

$$\frac{\sigma_y}{\sigma_{yS}} = c_{\sigma_y} \left(\frac{r}{l}\right)^3, \quad c_{\sigma_y} = \frac{3}{8}\sqrt{\frac{3}{2}}\pi \approx 1.4. \tag{A.5}$$

References

[1] Li R, Sieradzki K. Phys Rev Lett 1992;68:1168.
[2] Erlebacher J, Aziz M, Karma A, Dimitrov N, Sieradzki K. Nature 2001;410:450.
[3] Weissmüller J, Newman R, Jin HJ, Hodge A, Kysar J. MRS Bull 2009;34:577.
[4] Ding Y, Chen M. MRS Bull 2009;34:569.
[5] Snyder J, Fujita T, Chen M, Erlebacher J. Nat Mater 2010;9:904.
[6] Wittstock A, Zielasek V, Biener J, Friend C, Bäumer M. Science 2010;327:319.
[7] Wang L, Zhong Y, Widmann D, Weissmüller J, Behm R. Chemcatchem 2012;4:251.
[8] Kramer D, Viswanath R, Weissmüller J. Nano Lett 2004;4:793.
[9] Biener J, Wittstock A, Zepeda-Ruiz L, Biener M, Zielasek V, Kramer D, et al. Nat Mater 2009;8:47.
[10] Jin H, Wang X, Parida S, Wang K, Seo M, Weissmüller J. Nano Lett 2010;10:187.
[11] Chen L, Fujita T, Chen M. Electrochim Acta 2012;67:1.
[12] Biener J, Hamza A, Hodge A. Deformation behavior of nanoporous metals. Micro and nano mechanical testing of materials and devices. New York: Springer; 2008.
[13] Hodge AM, Biener J, Hayes JR, Bythrow PM, Volkert CA, Hamza AV. Acta Mater 2007;55:1343.
[14] Gibson L, Ashby M. Cellular solids: structure and properties. 2nd ed. Cambridge: Cambridge University Press; 1997.
[15] Uchic M, Dimiduk D, Florando J, Nix W. Science 2004;305:986.
[16] Greer J, Oliver W, Nix W. Acta Mater 2005;53:1821.
[17] Volkert C, Lilleodden E, Kramer D, Weissmüller J. Appl Phys Lett 2006;89:061920.
[18] Sun XY, Xu GK, Li X, Feng XQ, Gao H. J Appl Phys 2013;113:023505.
[19] Farkas D, Caro A, Bringa E, Crowson D. Acta Mater 2013;61:3249.
[20] Jin H, Kurmanaeva L, Schmauch J, Rosner H, Ivanisenko Y, Weissmüller J. Acta Mater 2009;57:2665.
[21] Jin H, Weissmüller J. Science 2011;332:1179.
[22] Wang K, Weissmüller J. Adv Mater 2013;25:1280.
[23] Ashby M, Bréchet Y. Acta Mater 2003;51:5801.
[24] Roberts A, Garboczi E. J Mech Phys Solids 2002;50:33.
[25] Feng XQ, Xia R, Li X, Li B. Appl Phys Lett 2009;94:011916.
[26] Liu R, Antoniou A. Acta Mater 2013;61:2390.
[27] Eggertsen PA, Mattiasson K. Int J Mater Form 2010;3:127.
[28] Abaqus theory manual V6.11. Providence (RI): Dassault Systèmes; 2011.
[29] Dou R, Derby B. Philos Mag 2011;91:1070.
[30] Greer J, Nix W. Phys Rev B 2006;73:245410.
[31] Kurmanaeva L, Ivanisenko Y, Markmann J, Fecht H, Weissmuller J. Phys Status Solidi-R 2010;4:130.
[32] Li L, Anderson P, Lee M, Bitzek E, Derlet P, Van Swygenhoven H. Acta Mater 2009;57:812.
[33] Parida S, Kramer D, Volkert C, Rosner H, Erlebacher J, Weissmueller J. Phys Rev Lett 2006;97:035504.
[34] Farkas D, Crowson D, Corcoran S. Scripta Mater 2009;61:497.
[35] Hodge AM, Doucette RT, Biener MM, Biener J, Cervantes O, Hamza AV. J Mater Res 2009;24:1600.